Remnants of shifting early Cenozoic Pacific lower mantle flow imaged beneath the Philippine Sea Plate

Jianke Fan [1,2] ✉, Dapeng Zhao [3], Cuilin Li [1,2] ✉, Lijun Liu [4] & Dongdong Dong [1,2]

Seismic anisotropy could provide vital information about the evolution and internal convection of the deep Earth interior. Although previous seismological studies have revealed a wide distribution of seismic anisotropy in the upper portion of the lower mantle beneath many subduction zones, the existence of anisotropy at these depths away from subducted slabs remains debated. Here we use P-wave azimuthal anisotropy tomography to image the crust and mantle down to 1,600-km depth. We find prominent anisotropic patterns in the upper portion of the lower mantle beneath the Philippine Sea Plate. Substantial azimuthal anisotropy with N–S fast-velocity directions occurs at 700–900-km depths. We interpret this azimuthal anisotropy as a remnant of the Pacific lower mantle flow field about 50 million years ago. Two isolated high-velocity anomalies at 700–1,600-km depths may be vestigial pieces of the subducted Izanagi slab with seismic velocity features suggesting a shift in the Pacific lower mantle flow field by about 40 million years ago. Our findings provide seismic evidence for the existence of complex lower mantle flows and deformation mechanisms away from subduction zones.

As an important layer, the lower mantle may play a critical role in the evolution and material cycle of the Earth interior. Therefore, it is important to better understand geodynamics of the lower mantle. It has been widely accepted that plate subduction and mantle plumes are two main styles in the evolution and material cycle of the Earth's surface and interior, which have been proven by global seismic tomography[1,2]. In these processes, the lower mantle is of great importance, which is not only the eventual destination of subducted slabs but also the birthplace of mantle plumes[3]. However, our knowledge on the geodynamical property of the lower mantle is still deficient.

As a valuable and useful tool in understanding geodynamics of the deep Earth processes, seismic anisotropy has been widely used to characterize deformations of the crust and lithosphere and flows in the mantle, providing vital information on the evolution and internal convection of the deep Earth interior, particularly in subduction zones[4,5]. Compared with the crust and upper mantle that are generally considered to be seismically anisotropic, most parts of the lower mantle are regarded to be seismically isotropic, although highly anisotropic minerals, such as bridgmanite and ferropericlase, are generally considered to be the major ingredients in the lower mantle[6,7]. This may depend on the predominant deformation mechanisms, such as diffusion or superplastic creep[8,9] and/or pure climb creep[10] in the bulk of the lower mantle.

To date, some shear-wave splitting measurements have suggested the presence of prominent seismic anisotropy in the upper portion of the lower mantle (UPLM) beneath several subduction zones[11–15]. In addition, a whole-mantle shear-wave anisotropic model suggests a wide

[1]CAS Key Laboratory of Marine Geology and Environment, Center of Ocean Mega-Science, Institute of Oceanology, Chinese Academy of Sciences, Qingdao, China. [2]Laboratory for Marine Geology, Qingdao National Laboratory for Marine Science and Technology, Qingdao, China. [3]Department of Geophysics, Graduate School of Science, Tohoku University, Sendai, Japan. [4]State Key Laboratory of Lithospheric Evolution, Institute of Geology and Geophysics, Chinese Academy of Sciences, Beijing, China. ✉e-mail: fanjianke@qdio.ac.cn; cuilinli@qdio.ac.cn
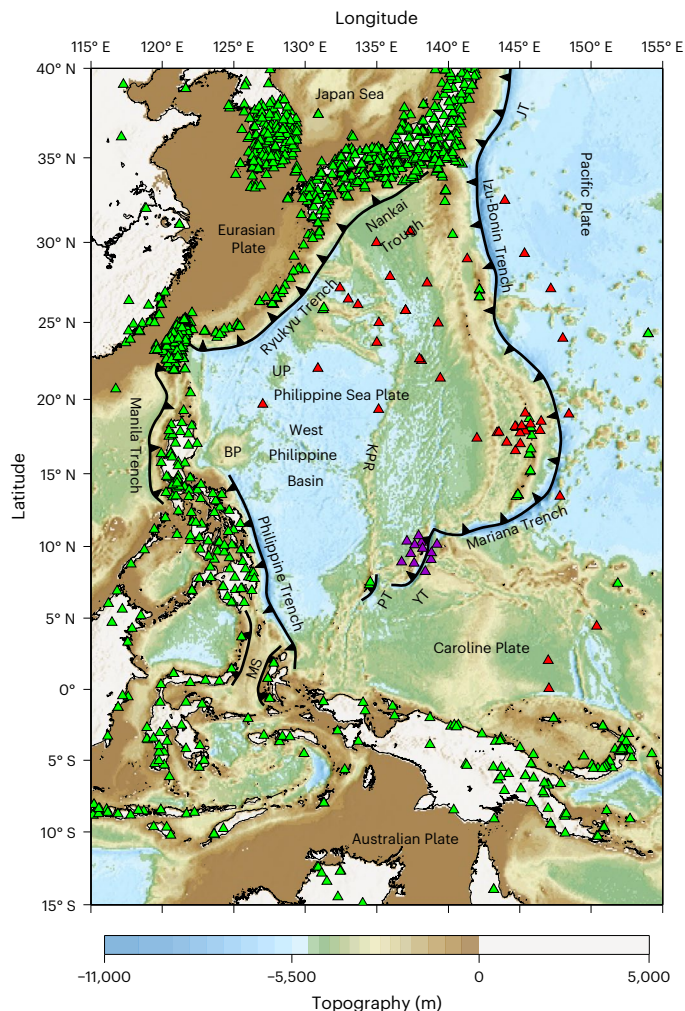
Fig. 1 | Tectonic settings in and around the PSP and distribution of seismic stations used in this study. The scale of the bathymetric data[44] is shown at the bottom. Seismic stations are shown as triangles. The serrated lines represent trench axes, which are generally determined based on the maximum water depth. The green, red and purple triangles denote the land-based stations from the International Seismological Centre[45], ocean bottom seismometers of the Ocean Hemisphere Project[46] and our ocean bottom seismometers deployed in the Yap area[47], respectively. BP, Benham Plateau; JT, Japan Trench; KPR, Kyushu Palau Ridge; MS, Molucca Sea; PT, Palau Trench; UP, Urdaneta Plateau; YT, Yap Trench.

distribution of seismic anisotropy in the UPLM beneath major subduction zones[16]. A mechanism of dislocation creep deformation caused by slab subduction is proposed to largely account for the UPLM seismic anisotropy[17,18]. However, these observations mainly focused on the vicinity of subducted slabs; the existence of seismic anisotropy away from the subducted slabs in the UPLM is still highly debated.

The Philippine Sea Plate (PSP) surrounded by subduction zones (Fig. 1) provides a valuable area to study the seismic structure and geodynamics away from the subducted slabs in the UPLM because of the extremely high seismicity. Many studies of seismic anisotropy in and around the PSP have been made[19–25], which have provided important information on the structure, dynamics and evolution of the PSP. However, up to now, seismic anisotropy in the UPLM beneath the PSP has not been revealed.

Azimuthal anisotropy in the UPLM beneath the PSP

In this work, we conducted P-wave azimuthal anisotropy tomography to image the detailed three-dimensional (3-D) anisotropic structure of the crust and mantle down to 1,600-km depth beneath the PSP. Our

tomographic images at different depths exhibit complex azimuthal anisotropy patterns (Fig. 2a–f and Supplementary Fig. 1), which are generally consistent with the previous results[19–25]. The most prominent feature of our azimuthal anisotropy tomography is N–S fast-velocity directions (FVDs) at depths of 700–900 km beneath the middle PSP, which are bounded by NW–SE FVDs to the northeast beneath the northern PSP (Fig. 2a–c). The NW–SE FVDs beneath the northern PSP extend from 300- to 1,600-km depths (Fig. 2a–f and Supplementary Fig. 1e–h), suggesting that the upper and lower mantle flow fields beneath the Pacific Plate are moving northwestward simultaneously. The different FVD features in the UPLM beneath the middle PSP and the Pacific Plate indicate that the present mantle flow patterns beneath the two plates are distinct.

Remnant of the Pacific lower mantle flow field 50 million years ago

The prominent N–S FVDs at 700–900-km depths beneath the middle PSP (Fig. 2a–c) seem to be less affected by the slab subduction because they occur generally away from the present subduction zones. In addition, previous seismic anisotropy studies revealed that the UPLM is generally characterized by trench-parallel FVDs[11–16], which are possibly caused by interactions between the subducted slab and the lower mantle inducing high differential stresses and dislocation creep[16]. Similarly, surface-wave anisotropic tomography revealed prominent anisotropies in the UPLM away from subduction zones beneath central Asia[26]. But they were still suggested to be connected with subducted slabs, because they are located in a large high-velocity (high-V) anomaly and may reflect strong interactions between the subducted Tethys, Izanagi and Pacific plates[26]. Different from central Asia, no high-V anomaly appears in the area where the prominent N–S FVDs are revealed by our azimuthal anisotropy tomography (Fig. 2a–c). Hence, we infer that these N–S FVDs are independent of the slab subduction.

Another proposed cause of the UPLM anisotropy is lateral lower mantle flow associated with a mantle plume[14]. A recent study of P-wave azimuthal anisotropy tomography has revealed similar N–S FVDs in a large-scale low-velocity (low-V) anomaly at depths of 1,300–1,600 km beneath Borneo, Southeast Asia[27], which are approximately parallel to the subduction direction and possibly reflect lateral movement of a mantle plume beneath the Java subduction zone[28]. This tomography also shows large high-V anomalies above the N–S FVDs, which reflect subducted slabs. This result may further indicate that the rising of the mantle plume beneath the Java subduction zone is impeded by the subducted slabs and results in the lateral mantle flow and the N–S FVDs. However, our tomography does not disclose a prominent low-V anomaly at 700–1,600-km depths beneath the PSP (Fig. 2a–f and Supplementary Fig. 3). If the N–S FVDs in our tomography were generated by lateral movement of a low-V anomaly, the lower mantle material would rise through the mantle transition zone and arrive at the PSP seafloor, simply because there is no subducted slab indicated by a high-V anomaly in the mantle transition zone beneath the southern PSP (Supplementary Figs. 1g,h and 2g,h). Thus, if a low-V mantle plume exists in the UPLM there, its rising would not be blocked. Nevertheless, geochemical studies have shown that basalts related to a mantle plume exist only in the Benham and Urdaneta plateaus[29,30] between 35 and 40 million years ago (Ma), suggesting that the mantle plume may have been inactive since then. Therefore, we deem that possible lateral flow of the lower mantle material may have contributed little to our observed N–S FVDs.

Some geodynamic simulations suggested that complete subduction and detachment of the Izanagi Plate induced an important transformation of the lower mantle flow beneath the Pacific Plate, from slow southward motion at 60 Ma to fast northward motion at 50 Ma, and further to be northwestward at 40 Ma[31]. The NW–SE FVDs at 300–1,600-km depths beneath the northern PSP (Fig. 2 and Supplementary Fig. 1e–h) and the N–S FVDs at 700–900-km depths beneath
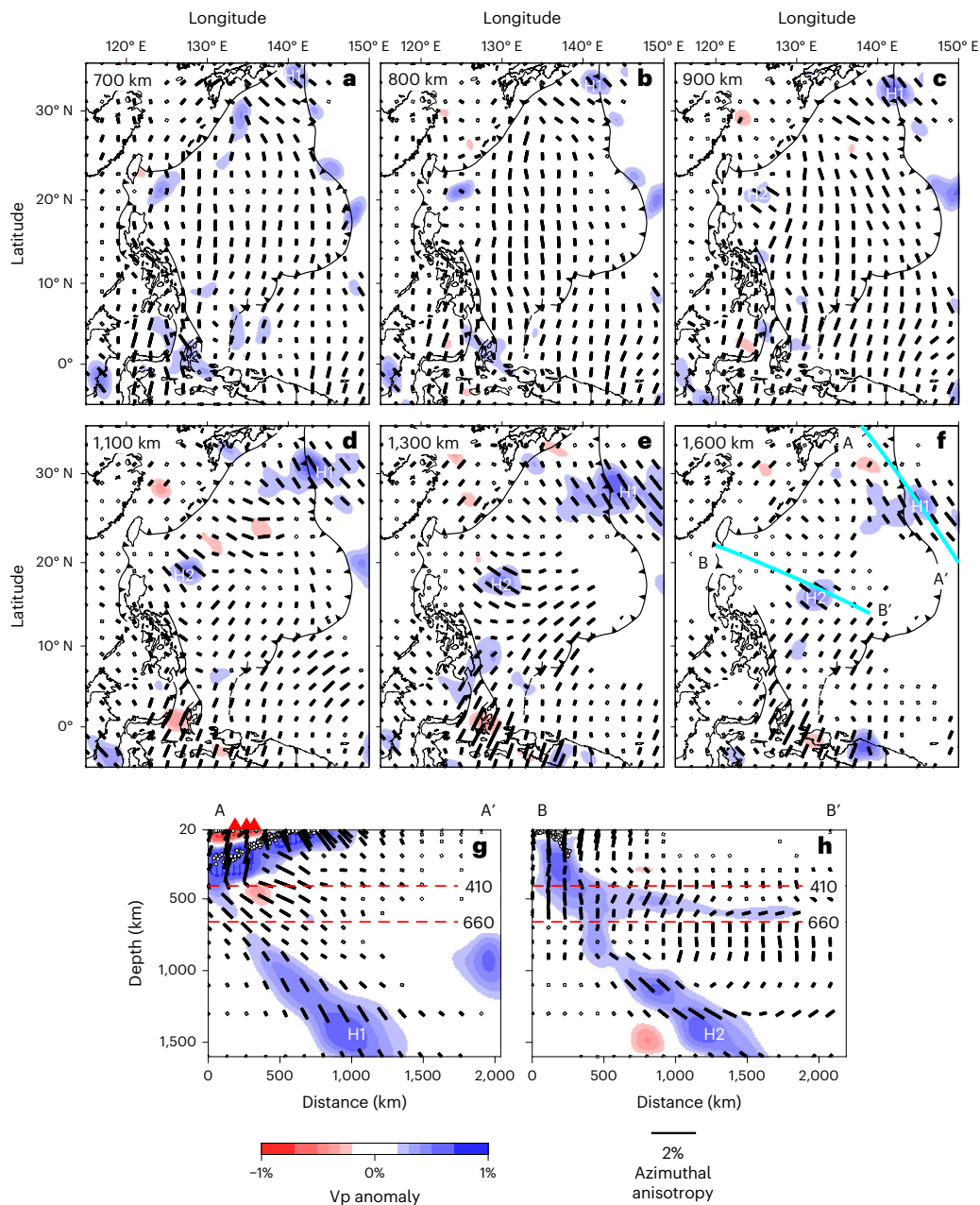
Fig. 2 | Map views and vertical cross sections of P-wave azimuthal anisotropic velocity tomography. a–h, Map views (**a–f**) and vertical cross sections (**g,h**) of P-wave azimuthal anisotropic velocity tomography. The layer depth is shown at the upper left corner of each map. Locations of the vertical cross sections are shown in **f**. The orientation and length of the black bars represent the fast-velocity direction and amplitude of azimuthal anisotropy, respectively, whose amplitude scale is shown at the bottom. Note that in **g** and **h**, the vertical bars denote N–S fast-velocity directions, whereas the horizontal bars denote E–W fast-velocity directions. White dots and red triangles in **g** and **h** show local seismicity and active volcanoes, respectively, within a 30-km width of each profile. Vp, P-wave velocity. H1 and H2 denote two high-V anomalies inferred to be the remnants of the subducted Izanagi slab. Other symbols are the same as those in Fig. 1.

the middle PSP revealed by our anisotropy tomography are highly consistent with the northwestward and northward movements of the lower mantle flow beneath the Pacific Plate at 40 and 50 Ma, respectively, as suggested by those geodynamic simulations. Therefore, we infer that the NW–SE FVDs at 300–1,600-km depths may further reflect the stable northwestward movement of the upper and lower mantle flow fields beneath the Pacific Plate since about 40 Ma, and the N–S FVD at 700–900-km depths beneath the middle PSP is an indicator of the remnant Pacific lower mantle flow field at about 50 Ma (Fig. 3).

Seismological studies detected seismic scatterers at 1,000–1,800-km depths under east of the Izu–Bonin–Mariana Trench

(Supplementary Fig. 3d–f), which are suggested to be an ancient subducted oceanic slab and not related with the contemporary subducting Pacific slab along the Izu–Bonin–Mariana Trench[32,33]. They may be carried northward 500–1,000 km from the present Mariana Trench due to oblique subduction[34]. These seismic scatterers are in good accordance with one high-V anomaly at 1,100–1,600-km depths beneath the southern Izu–Bonin Trench revealed by our isotropic tomography (H1 in Supplementary Fig. 3d–f), which also shows that H1 is disconnected with the subducting Pacific slab along the Izu–Bonin–Mariana Trench (Supplementary Fig. 4). Hence, H1 probably reflects the ancient subducted oceanic slab. Similar features were also observed
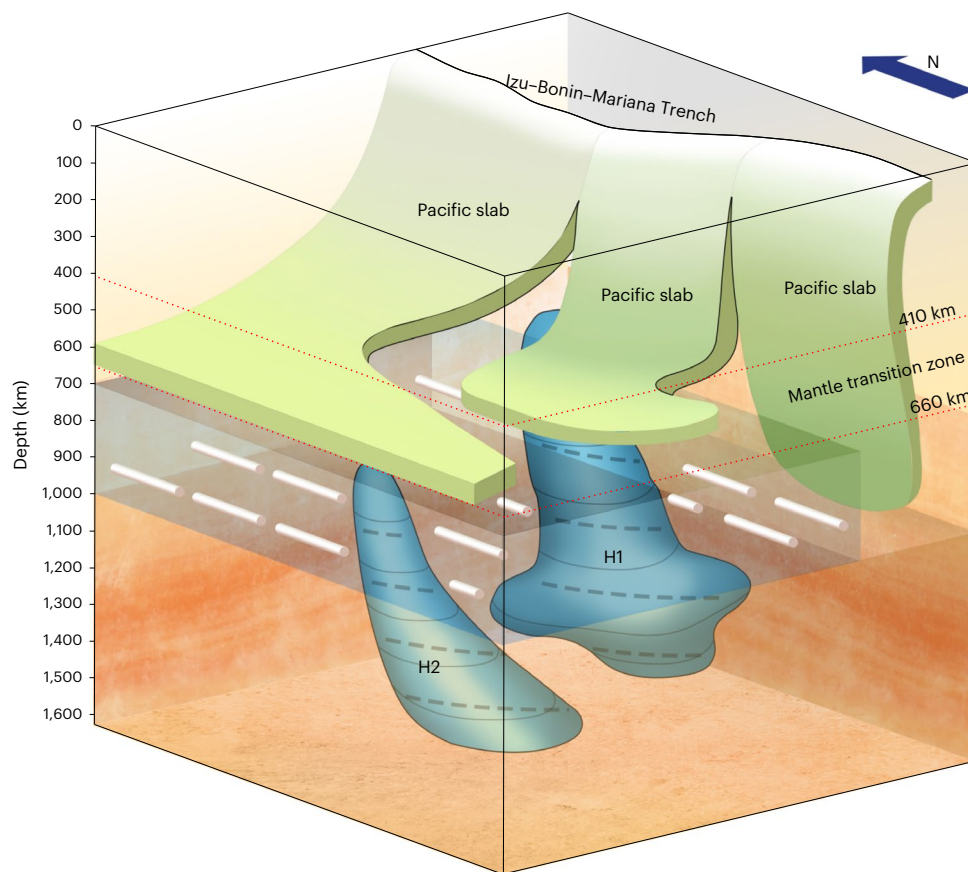
Fig. 3 | A schematic diagram showing remnants of the early Cenozoic Pacific lower mantle flow beneath the Philippine Sea Plate. The white bars and grey dashed lines denote remnants of the Pacific lower mantle flow field at about 50 Ma and 40 Ma, respectively.

at 930–1,120 km depths beneath Northeast China and the adjacent Japan Sea, which are suggested to be a piece of remnant of the subducted Izanagi slab before the present subducting Pacific slab along the Izu–Bonin–Mariana Trench[35]. Consequently, we suggest that H1 is another piece of remnant of the subducted Izanagi slab, whose time to sink down to ~1,000-km depth was estimated to be 45–60 million years[35]. This timescale coincides well with some plate reconstruction results based on tomographic results along the Mariana Trench[36]. They suggest that the Mariana Trench has been at its present location (with ±200-km uncertainties) since the subduction initiation of the Pacific Plate beneath the PSP in the early Cenozoic, because tomographic results show that the subducted Pacific slab along the Mariana Trench has a length of over 1,000 km[36]. This argument is supported by the location of H1 and its separation from the subducting Pacific slab along the Izu–Bonin–Mariana Trench, considering that H1 may have moved northwards for a distance of 500–1,000 km[34]. Hence, we infer that the Pacific Plate has been continuously subducting along the Mariana Trench since the early Cenozoic. When the subducted Pacific slab from the Mariana Trench reached the UPLM, the lower mantle flow field at 700–900-km depths beneath the PSP would be separated from and not influenced by that beneath the Pacific Plate, leading to the maintenance of the remnant of the Pacific lower mantle flow from about 50 Ma to the present.

Remnant of the Pacific lower mantle flow field at about 40 Ma

Besides H1 (Fig. 2a–g), another isolated high-V anomaly (H2 in Fig. 2c–f,h) is also characterized by similar NW–SE FVDs. The locations of H1 and H2 are generally consistent with that of the spreading centre between the Izanagi and Pacific plates when this spreading centre was

about to subduct beneath the Eurasian Plate[37]. Thus, we infer that H2 is another remnant of the subducted Izanagi slab.

The NW–SE FVDs in H1 (Fig. 2) may reflect the stable northwestward movement of the lower mantle flow field beneath the Pacific Plate since ~40 Ma because the NW–SE FVDs in H1 are consistent with those in the upper mantle and the mantle transition zone (Supplementary Fig. 1e–h). However, the NW–SE FVDs in H2 are greatly different from those in the surrounding lower mantle at the same depths and those at the same location in the upper mantle and the mantle transition zone (Fig. 2c–f and Supplementary Fig. 1), which may indicate that the anisotropy in H2 is not influenced by the present lower mantle flow. Considering that H1 and H2 are not connected, and both of them are remnants of the subducted Izanagi slab with similar anisotropic features, we infer that H2 possibly preserves the remnant of the Pacific lower mantle flow field at about 40 Ma (Fig. 3). This may be ascribed to the amorphous mantle flow field around H2 as shown by the slightly disordered FVDs around H2 at 900–1,600-km depths (Fig. 2c–f). Hence, H2 may not have experienced phase transition associated with mantle convection but preserve its fossil frozen-in anisotropy.

The above process is analogous to the preservation of primitive mantle materials in the lower mantle. Recent geodynamic models suggest that intrinsically stable and strong bridgmanite-enriched ancient mantle structures (BEAMSs) exist in the lower mantle, which could sustain the lateral heterogeneity of the lower mantle for billions of years and are less affected by subducting slabs and mantle plumes[38]. The existence of the primitive mantle materials is also suggested by mineral physics and geochemical studies[39–41]. Recent studies have suggested that these BEAMSs may have a high viscosity contrast of ~10–50 times in the deep mantle reservoir with a small scale[42] and a grain size less than several hundred micrometres[43] to retain their primordial

signature. The small-scale trait of these BEAMSs may allow them to be carried by mantle flow and move to the surface or other places in the Earth[40]. Although the primitive mantle materials in the lower mantle are not revealed by this study, our anisotropic tomography shows that the former lower mantle flow field can be maintained for dozens of millions years, suggesting that the preservation of primitive mantle materials in the lower mantle for several billion years is quite possible.

Our anisotropic tomography suggests that seismic anisotropy in the lower mantle may be much more prevalent than previously thought, not only in the vicinity of the subducting slabs but also away from the slabs. The clear UPLM anisotropy we observed further suggests that dislocation creep may play a more important role in the deep Earth interior than commonly believed. These observations also provide important and independent seismic evidence for the existence of past deformations within the lower mantle, which may stimulate future geodynamical modelling to better understand the deformation mechanisms, rheology and thermodynamic and thermoelastic properties of minerals in the deep mantle.

Online content

Any methods, additional references, Nature Portfolio reporting summaries, source data, extended data, supplementary information, acknowledgements, peer review information; details of author contributions and competing interests; and statements of data and code availability are available at https://doi.org/10.1038/s41561-024-01404-6.

References

1. van der Hilst, R., Widiyantoro, S. & Engdahl, E. Evidence for deep mantle circulation from global tomography. *Nature* **386**, 578–584 (1997).
2. Zhao, D. Seismic structure and origin of hotspots and mantle plumes. *Earth Planet. Sci. Lett.* **192**, 251–265 (2001).
3. Garnero, E. J. & McNamara, A. K. Structure and dynamics of Earth's lower mantle. *Science* **320**, 626–628 (2008).
4. Long, M. D. Constraints on subduction geodynamics from seismic anisotropy. *Rev. Geophys.* **51**, 76–112 (2013).
5. Zhao, D., Liu, X., Wang, Z. & Gou, T. Seismic anisotropy tomography and mantle dynamics. *Surv. Geophys.* **44**, 947–982 (2023).
6. Wang, X., Tsuchiya, T. & Hase, A. Computational support for a pyrolitic lower mantle containing ferric iron. *Nat. Geosci.* **8**, 556–559 (2015).
7. Kurnosov, A., Marquardt, H., Frost, D. J., Ballaran, T. B. & Ziberna, L. Evidence for a Fe^{3+}-rich pyrolitic lower mantle from (Al,Fe)-bearing bridgmanite elasticity data. *Nature* **543**, 543–546 (2017).
8. Karato, S. I. & Li, P. Diffusion creep in perovskite: implications for the rheology of the lower mantle. *Science* **255**, 1238–1240 (1992).
9. Karato, S. I., Zhang, S. & Wenk, H. R. Superplasticity in Earth's lower mantle: evidence from seismic anisotropy and rock physics. *Science* **270**, 458–461 (1995).
10. Boioli, F. et al. Pure climb creep mechanism drives flow in Earth's lower mantle. *Sci. Adv.* **3**, e1601958 (2017).
11. Foley, B. J. & Long, M. D. Upper and mid-mantle anisotropy beneath the Tonga slab. *Geophys. Res. Lett.* **38**, L02303 (2011).
12. Lynner, C. & Long, M. D. Sub-slab anisotropy beneath the Sumatra and circum-Pacific subduction zones from source-side shear wave splitting observations. *Geochem. Geophys. Geosyst.* **15**, 2262–2281 (2014).
13. Wookey, J., Kendall, J. M. & Barruol, G. Mid-mantle deformation inferred from seismic anisotropy. *Nature* **415**, 777–780 (2002).
14. Wookey, J. & Kendall, J. M. Evidence of midmantle anisotropy from shear wave splitting and the influence of shear-coupled P wave. *J. Geophys. Res.* **109**, B07309 (2004).
15. Zhu, H., Stern, R. J. & Yang, J. Seismic evidence for subduction-induced mantle flows underneath Middle America. *Nat. Commun.* **11**, 2075 (2020).
16. Ferreira, A. M. G., Faccenda, M., Sturgeon, W., Chang, S. J. & Schardong, L. Ubiquitous lower-mantle anisotropy beneath subduction zones. *Nat. Geosci.* **12**, 301–306 (2019).
17. Cordier, P., Ungár, T., Zsoldos, L. & Tichy, G. Dislocation creep in MgSiO$_3$ perovskite at conditions of the Earth's uppermost lower mantle. *Nature* **428**, 837–840 (2004).
18. Tsujino, N. et al. Mantle dynamics inferred from the crystallographic preferred orientation of bridgmanite. *Nature* **539**, 81–84 (2016).
19. Fan, J. & Zhao, D. P-wave anisotropic tomography of the central and southern Philippines. *Phys. Earth Planet. Inter.* **286**, 154–164 (2019).
20. Fan, J. & Zhao, D. P-wave tomography and azimuthal anisotropy of the Manila–Taiwan–Southern Ryukyu region. *Tectonics* **40**, e2020TC006262 (2021).
21. Isse, T. et al. Anisotropic structures of the upper mantle beneath the northern Philippine Sea region from Rayleigh and Love wave tomography. *Phys. Earth Planet. Inter.* **183**, 33–43 (2010).
22. Ma, J., Tian, Y., Zhao, D., Liu, C. & Liu, T. Mantle dynamics of Western Pacific and East Asia: new insights from P-wave anisotropic tomography. *Geochem. Geophys. Geosyst.* **20**, 3628–3658 (2019).
23. Qiao, Q. et al. Upper mantle structure beneath Mariana: insights from Rayleigh-wave anisotropic tomography. *Geochem. Geophys. Geosyst.* **22**, e2021GC009902 (2021).
24. Wei, W., Zhao, D., Xu, J., Wei, F. & Liu, G. P and S wave tomography and anisotropy in Northwest Pacific and East Asia: constraints on stagnant slab and intraplate volcanism. *J. Geophys. Res.* **120**, 1642–1666 (2015).
25. Wei, W., Zhao, D., Yu, W. & Shi, Y. Complex patterns of mantle flow in eastern SE Asian subduction zones inferred from P-wave anisotropic tomography. *J. Geophys. Res.* **127**, e2021JB023366 (2022).
26. Montagner, J. P., Burgos, G., Capdeville, Y., Beucler, E. & Mocquet, A. The mantle transition zone dynamics as revealed through seismic anisotropy. *Tectonophysics* **821**, 229133 (2021).
27. Hua, Y., Zhao, D. & Xu, Y. G. Azimuthal anisotropy tomography of the Southeast Asia subduction system. *J. Geophys. Res.* **127**, e2021JB022854 (2022).
28. Mériaux, C. A. et al. Mantle plumes in the vicinity of subduction zones. *Earth Planet. Sci. Lett.* **454**, 166–177 (2016).
29. Ishizuka, O., Taylor, R. N., Ohara, Y. & Yuasa, M. Upwelling, rifting, and age-progressive magmatism from the Oki-Daito mantle plume. *Geology* **41**, 1011–1014 (2013).
30. Yan, Q., Shi, X., Yuan, L., Yan, S. & Liu, Z. Tectono-magmatic evolution of the Philippine Sea Plate: a review. *Geosyst. Geoenviron.* **1**, 100018 (2022).
31. Seton, M. et al. Ridge subduction sparked reorganization of the Pacific plate-mantle system 60-50 million years ago. *Geophys. Res. Lett.* **42**, 1732–1740 (2015).
32. Kaneshima, S. Seismic scatterers in the lower mantle near subduction zones. *Geophys. J. Int.* **219**, S2–S20 (2019).
33. Rost, S., Garnero, E. J. & Williams, Q. Seismic array detection of subducted oceanic crust in the lower mantle. *J. Geophys. Res.* **113**, B06303 (2008).
34. Castle, J. C. & Creager, K. C. A steeply dipping discontinuity in the lower mantle beneath Izu-Bonin. *J. Geophys. Res.* **104**, 7279–7292 (1999).
35. Li, J. & Yuen, D. A. Mid-mantle heterogeneities associated with Izanagi plate: implications for regional mantle viscosity. *Earth Planet. Sci. Lett.* **385**, 137–144 (2014).
36. Wu, J., Suppe, J., Lu, R. & Kanda, R. Philippine Sea and East Asian plate tectonics since 52 Ma constrained by new subducted slab reconstruction methods. *J. Geophys. Res.* **121**, 4670–4741 (2016).
37. Müller, R. D. et al. Ocean basin evolution and global-scale plate reorganization events since Pangea breakup. *Annu. Rev. Earth Planet. Sci.* **44**, 107–138 (2016).

38. Ballmer, M. D., Houser, C., Hernlund, J. W., Wentzcovitch, R. M. & Hirose, K. Persistence of strong silica-enriched domains in the Earth's lower mantle. *Nat. Geosci.* **10**, 236–240 (2017).

39. Tsujino, N. et al. Viscosity of bridgmanite determined by in situ stress and strain measurements in uniaxial deformation experiments. *Sci. Adv.* **8**, eabm1821 (2022).

40. Rizo, H. et al. Preservation of Earth-forming events in the tungsten isotopic composition of modern flood basalts. *Science* **352**, 809–812 (2016).

41. Mukhopadhyay, S. Early differentiation and volatile accretion recorded in deep-mantle neon and xenon. *Nature* **486**, 101–104 (2012).

42. Liu, H., Leng, W., Wang, W. & Zheng, Y. Deciphering the deep Earth heterogeneities from the temperature fluctuation of mantle plumes. *Earth Planet. Sci. Lett.* **618**, 118275 (2023).

43. Deng, Z. et al. Earth's evolving geodynamic regime recorded by titanium isotopes. *Nature* https://doi.org/10.1038/s41586-023-06304-0 (2023).

44. Smith, W. H. F. & Sandwell, D. T. Global seafloor topography from satellite altimetry and ship depth soundings. *Science* **277**, 1957–1962 (1997).

45. Engdahl, E. R., van der Hilst, R. & Buland, R. Global teleseismic earthquake relocation with improved travel times and procedures for depth determination. *Bull. Seismol. Soc. Am.* **88**, 722–743 (1998).

46. Shiobara, H., Baba, K., Utada, H. & Fukao, Y. Ocean bottom array probes stagnant slab beneath the Philippine Sea. *EOS Trans. AGU* **90**, 70–71 (2009).

47. Fan, J. et al. Seismic structure of the Caroline Plateau-Yap Trench collision zone. *Geophys. Res. Lett.* **49**, e2022GL098017 (2022).

Methods

Data

The P-wave arrival-time data utilized in this study are comprised of three parts. The first part includes P-wave arrival-time data of local, regional and teleseismic events recorded at land-based stations (green triangles in Fig. 1) collected from the International Seismological Centre (ISC)-EHB database (http://www.isc.ac.uk/isc-ehb/search/arrivals/) from 1964 to 2019, in which all the events are well relocated using the EHB algorithm[45]. The second part consists of P-wave arrival-time data of local and regional earthquakes recorded at ocean bottom seismometers deployed by the Ocean Hemisphere Project[46] (red triangles in Fig. 1; http://ohpdmc.eri.u-tokyo.ac.jp/). The third part includes P-wave arrival-time data of local and regional earthquakes recorded at ocean bottom seismometers in the Yap subduction zone[47] (purple triangles in Fig. 1), which were deployed and retrieved by the Institute of Oceanology, Chinese Academy of Sciences, using the research Vessel KEXUE. The P-wave arrival times of local and regional events recorded at the ocean bottom seismometers are manually picked based on theoretical arrival times computed for the IASP91 Earth model[48] and merged with the ISC-EHB data.

Then we carefully sifted the data of local and regional events according to the following criteria: (1) each earthquake was recorded at more than four stations in the study region; (2) the arrivals with epicentral distance >200 km are used in the inversion, because we mainly focus on large-scale velocity structures of the mantle and (3) the absolute value of raw travel-time residuals is smaller than 2.5 s. Finally, our dataset contains 1,005,690 P-wave arrival times of 50,345 local and regional events recorded at 1,235 stations, including 1,635 arrivals at 56 ocean bottom seismometers (Supplementary Fig. 7a).

For the teleseismic events, the selection criteria are as follows: (1) each event was recorded at more than five seismic stations in the study region; (2) the absolute value of each travel-time residual is smaller than 3.0 s; (3) the epicentral distance between a teleseismic event and a station is in a range of 30–100°. As a result, 294,213 P-wave arrivals of 20,607 teleseismic events are selected to use in this study (Supplementary Fig. 7b).

Azimuthal anisotropic and isotropic tomographic inversions

To determine the 3-D azimuthal anisotropy and isotropic P-wave velocity (Vp) models beneath the PSP, we use the azimuthal anisotropic and isotropic tomographic methods[49,50]. In the anisotropic tomographic method, weak azimuthal anisotropy with a horizontal axis of hexagonal symmetry is assumed. Thus, P-wave slowness (that is, $1\,Vp^{-1}$) in an arbitrary propagation direction can be approximately expressed as:

$$S(\varnothing) = S_0(1 + A\cos(2\varnothing) + B\sin(2\varnothing)) \qquad (1)$$

where S is the total slowness, S_0 is isotropic slowness, A and B are two azimuthal anisotropy parameters, and $\varnothing$ is ray path azimuth. The fast-velocity direction (FVD) ψ and the azimuthal anisotropy amplitude α can be expressed as follows:

$$\psi = \begin{cases} \frac{1}{2}\tan^{-1}\left(\frac{B}{A}\right) + \begin{cases} \frac{\pi}{2}, & A > 0 \\ 0, & A < 0, \end{cases} \\ -\frac{\pi}{4}, & A = 0, \quad B > 0, \\ \frac{\pi}{4}, & A = 0, \quad B < 0, \end{cases} \qquad (2)$$

$$\alpha = \frac{\sqrt{A^2 + B^2}}{1 - (A^2 + B^2)},$$

For the isotropic tomography, 3-D grid nodes are arranged in the study volume with a lateral grid interval of 1.0°, whereas for the anisotropic tomography, 3-D grid nodes are set with a lateral grid interval of 2.0°, because compared to isotropic Vp tomography, a better

coverage of rays in azimuth and incident angle is required to obtain robust Vp anisotropic tomography. In the vertical direction, the grid nodes are set at depths of 20; 50; 100; 200; 300; 400; 500; 600; 700; 800; 900; 1,100; 1,300 and 1,600 km. We adopt an updated Vp model as the one-dimensional (1-D) initial model, which is integrated from the CRUST1.0 model[51], the WPSP01P model[52] and the IASP91 Earth model[48], similar to our previous studies[19,20]. The 1-D initial Vp model includes four velocity discontinuities, that is, the Conrad, Moho, 410 and 660 km discontinuities. Using this initial 1-D Vp model, we relocate all the local and regional earthquakes. Then we conduct the azimuthal anisotropy and isotropic tomographic inversions using the Least Squares with QR factorization (LSQR) algorithm[53] with damping and smoothing regularizations. Considering the trade-off between the root mean square (RMS) travel-time residual and the norm of a 3-D Vp model, the optimal damping and smoothing parameters are found to be 500.0 and 20,000.0, respectively (Supplementary Fig. 8), after conducting many tomographic inversions with different values of the damping and smoothing parameters. After the isotropic and anisotropic inversions (Supplementary Fig. 9), the RMS travel-time residual is reduced from 1.305 s for the initial 1-D Vp model to 1.075 s for the 3-D isotropic Vp model and further reduced to 1.034 s for the 3-D Vp azimuthal anisotropic model. The RMS residual reductions are found to be statistically significant after performing the F-test[19,54].

Resolution analysis

To evaluate the resolution and robustness of the main features of our azimuthal anisotropy tomographic model and the trade-off between the isotropic Vp and azimuthal anisotropy, we performed a number of chequerboard resolution tests (CRTs) and restoring resolution tests (RRTs). In the CRTs, three kinds of input models with different values of the isotropic Vp and azimuthal anisotropy parameters are constructed. In the first to third input models, the isotropic Vp perturbations are assigned to be ±2%, 0% and ±2%, whereas perturbations of the anisotropic parameters (A and B) are ±2%, ±2% and 0%, respectively. According to equation (2), the input FVDs at two neighbouring grid nodes are normal to each other with an amplitude of 2%. In the RRTs, four input models with different azimuthal anisotropy parameters are constructed: (1) N–S FVDs with an amplitude of 2% beneath the middle PSP at depths of 700–900 km; (2) E–W FVDs with an amplitude of 2% beneath the middle PSP at depths of 700–900 km; (3) NW–SE FVDs with an amplitude of 2% beneath the northeastern PSP at depths of 300–1,600 km and (4) NW–SE FVDs with an amplitude of 2% in the anomaly H2 at depths of 900–1,600 km. Then theoretical travel times are calculated for each input model, and the same ray paths as in the observed dataset are used. To simulate picking errors of the arrival-time data, we add Gaussian noise (−0.25 to +0.25 s) with a standard deviation of 0.1 s to the synthetic travel times, which are then inverted to obtain an output model. Comparing the input and output models, we can judge whether the input model can be well recovered or not.

Supplementary Figs. 10–25 show the obtained CRT and RRT results. The CRT results (Supplementary Figs. 10–13) indicate that the resolution is generally good beneath most of the study region, except for the central and marginal areas at depths of 20-300 km, where the seismic rays do not crisscross very well (Supplementary Fig. 26). The tomographic results, especially the azimuthal anisotropic images, have a spatial resolution of 2.0° at depths of 20–800 km and 4.0° at depths of 900–1,600 km (Supplementary Figs. 10–13). Supplementary Figs. 14–21 show the CRT results for assessing the trade-off between the isotropic Vp and azimuthal anisotropy, which indicate that the trade-off does exist but it mainly occurs in the marginal areas where the resolution is low due to the imperfect ray coverage. As a whole, the trade-off between the isotropic Vp and azimuthal anisotropy is insignificant, and our azimuthal anisotropy tomography is reliable. Four RRTs are performed to further evaluate the robustness of the main features of our isotropic Vp

and azimuthal anisotropy tomographic results, such as the N–S FVDs at depths of 700–900 km beneath the middle PSP (Supplementary Figs. 22–23), the NW–SE FVDs beneath the northeastern PSP at depths of 300–1,600 km (Supplementary Fig. 24) and the NW–SE FVDs in H2 beneath the middle PSP at depths of 900–1,600 km (Supplementary Fig. 25). These RRT results indicate that all the input isotropic Vp and azimuthal anisotropy patterns, including the amplitude and FVDs, can be generally well recovered. Although slight smearing occurs in some areas, it does not affect the main features of our tomography.

We further performed three more RRTs to investigate the effect of Vp radial anisotropy on the N–S FVDs at 700–900-km depths beneath the middle PSP. In these tests, the input models contain negative radial anisotropy (that is, vertical Vp > horizontal Vp) with an amplitude of 1% at 700–900-km and 20–600-km depths at 9–25° N latitudes and 20–1,100-km depths at 9–35° N, respectively. Then we conducted azimuthal anisotropic inversions. The test results (Supplementary Figs. 27–29) show that although some artifacts of isotropic Vp and azimuthal anisotropy show up at some depths, they are quite different from our results of isotropic Vp and azimuthal anisotropy. Hence, the N–S FVDs at 700–900-km depths beneath the middle PSP are not caused by radial anisotropy.

Data availability
The P-wave arrival-time data used in this study are available at http://www.isc.ac.uk/isc-ehb/search/arrivals/, https://doi.org/10.12157/IOCAS.20211110.002, http://ohpdmc.eri.u-tokyo.ac.jp and https://doi.org/10.12157/IOCAS.20230828.001. The 3-D velocity model can be requested from the corresponding authors.

Code availability
The free software GMT (https://www.generic-mapping-tools.org/) was used in this study. The analysis codes and related scripts for generating figures used in the main text and Supplementary Information are available from the corresponding authors upon reasonable request.

References

48. Kennett, B. & Engdahl, E. R. Traveltimes for global earthquake location and phase identification. *Geophys. J. Int.* **105**, 429–465 (1991).
49. Wang, J. & Zhao, D. P-wave anisotropic tomography beneath Northeast Japan. *Phys. Earth Planet. Inter.* **170**, 115–133 (2008).
50. Zhao, D., Hasegawa, A. & Kanamori, H. Deep structure of Japan subduction zone as derived from local, regional and teleseismic events. *J. Geophys. Res.* **99**, 22313–22329 (1994).
51. Laske, G., Masters, G., Ma, Z. & Pasyanos, M. Update on CRUST1.0—a 1-degree global model of Earth's CRUST. *Geophys. Res. Abstr.* **15**, 2013–2658 (2013).
52. Wright, C. & Kuo, B. Evidence for an elevated 410 km discontinuity below the Luzon, Philippines region and transition zone properties using seismic stations in Taiwan and earthquake sources to the south. *Earth Planets Space* **59**, 523–539 (2007).
53. Paige, C. C. & Saunders, M. A. LSQR: an algorithm for sparse linear equations and sparse least squares. *ACM Trans. Math. Software* **8**, 43–71 (1982).
54. Zhao, D. *Multiscale Seismic Tomography* (Springer, 2015).

Acknowledgements

Author contributions
J.F. and C.L. conceived this study. C.L. and D.D. collected the data and implemented data processing. D.Z. developed the tomographic codes. J.F. conducted the tomographic inversions. All authors contributed to the interpretations and preparations of the manuscript.

Competing interests
The authors declare no competing interests.

Additional information
Supplementary information The online version contains supplementary material available at https://doi.org/10.1038/s41561-024-01404-6.

Correspondence and requests for materials should be addressed to Jianke Fan or Cuilin Li.

Peer review information *Nature Geoscience* thanks the anonymous reviewers for their contribution to the peer review of this work. Primary Handling Editors: Alison Hunt and James Super, in collaboration with the *Nature Geoscience* team.

Reprints and permissions information is available at www.nature.com/reprints.